ROYAL SOCIETY
OF CHEMISTRY

PAPER

CrossMark
click for updates

Spectral shifting and NIR down-conversion in Bi^{3+}/Yb^{3+} co-doped Zn$_2$GeO$_4$

Guojun Gao,[a] Mingying Peng[bc] and Lothar Wondraczek*[ac]

We report on spectral modification through NIR down-conversion (DC) photoluminescence (PL) in Yb^{3+}-Bi^{3+}-co-doped Zn$_2$GeO$_4$. Energetic downshifting (DS) of UV-A irradiation occurs *via* intrinsic luminescence of the high-bandgap semiconductor Zn$_2$GeO$_4$ as well as *via* active Bi^{3+} centres. In parallel, both species act as sensitizers for Yb^{3+}, strongly extending its excitation region to ~500 nm. In the absence of Bi^{3+}, band-to-band absorption of Zn$_2$GeO$_4$ in the UV region results in PL at ~475–625 nm. Doping with Yb^{3+} initiates energy transfer from trapped defect states to two neighbouring Yb^{3+} ions in a cooperative DC process, resulting in Yb^{3+}-related photoemission at ~1000 nm. The introduction of Bi^{3+} into Zn$_2$GeO$_4$:Yb^{3+} greatly extends the absorption band to the visible blue region. Then, energy transfer also occurs through cooperative DC from Bi^{3+} to Yb^{3+}. As a result, a strong increase in the absolute Yb^{3+}-related PL intensity is observed. This enables ultra-efficient harvesting of UV-A to visible radiation for energy conversion processes.

Introduction

The spectral conversion of incident sunlight through photoluminescence has been proposed to enhance the efficiency of various solar energy harvesting processes.[1–7] For example, in the case of crystalline silicon solar cells, a large fraction of the incoming solar energy is lost either because photons do not surpass the energy gap which is necessary to generate a photoelectron (NIR-tail of the solar spectrum), or because their excess energy causes thermalization or electron–hole recombination (near-UV to green part of the solar spectrum). Conversion strategies consequently follow some straightforward schemes: for example, in up-conversion processes (UC), two or more low-energy photons are used to generate one photon of higher energy. In down-shifting (DS) or quantum cutting (QC) processes, on the other side, a high-energy photon is converted into one (DS) or more (QC) photons of lower energy.[1,2,8–12] In the latter, a quantum efficiency which is theoretically higher than unity can be achieved. As a concept, all three processes enable to adjust the incoming solar spectrum through increasing the number of photons within a certain spectral region. Whether or not this is advantageous for a specific solar energy conversion process, however, depends on many other factors, including

quantum efficiency, secondary absorption processes, converter properties, system design and cost.

Here, we concentrate on the model system of Zn$_2$GeO$_4$:Yb^{3+} and its further sensitization with Bi^{3+} co-dopants. Yb^{3+} has a rather simple band structure with the single excited state of $^2F_{5/2}$ at an energy of ~1 eV. Yb^{3+} photoluminescence therefore occurs at a wavelength of ~1000 nm, which is very close to the maximum photoelectronic conversion efficiency of silicon. Hence, trivalent ytterbium is an often-sought emitter for solar spectral conversion through QC or DS.[1–4] For this, a suitable sensitizer is required which adds favourable absorption properties to the emission behaviour of Yb^{3+}. Most of the trivalent rare earth (RE^{3+}) ions, *e.g.*, Pr^{3+}, Er^{3+}, Nd^{3+}, Ho^{3+}, Tb^{3+}, Tm^{3+} and Dy^{3+} have been considered for this purpose.[1,2,8–19] However, the parity-forbidden 4f^n → 4f^n transitions in these ions typically result in weak and narrow absorption bands which stand in contrast to the wish for efficient (broadband) harvesting of sunlight. As alternatives, ions such as Ce^{3+}, Eu^{2+}, Bi^{3+} and Mn^{2+}, and/or combination with intrinsic absorption of the host itself (*e.g.*, YVO$_4$ and ZnO) have therefore been studied for Yb^{3+} activation.[20–24]

The orthogermanate of zinc, Zn$_2$GeO$_4$, is a wide-bandgap semiconductor with a gap-energy of ~4.68 eV.[25] Without further dopants, it exhibits broadband luminescence in the blue to green spectral region which originates from the recombination of native structural defects.[26,27] Emission from Zn$_2$GeO$_4$ occurs at about twice the energy which is necessary to excite Yb^{3+}: $^2F_{7/2}$ → $^2F_{5/2}$. This means that it can be used to sensitize Yb^{3+}. On the other hand, absorption covers only the UV region of ~250 to 350 nm, which prevents efficient solar harvesting. To overcome this, we introduce trivalent bismuth as further activator into the

[a]Otto Schott Institute of Materials Research, University of Jena, 07743 Jena, Germany. E-mail: lothar.wondraczek@uni-jena.de

[b]State Key Laboratory of Luminescent Materials and Devices, School of Materials Science and Technology, South China University of Technology, 510641 Guangzhou, China

[c]The Chinese-German Research Center for Photonic Materials and Devices at South China University of Technology, 510641 Guangzhou, China

This journal is © The Royal Society of Chemistry 2014

J. Mater. Chem. C, 2014, **2**, 8083–8088 | 8083

Zn_2GeO_4 host. Bi^{3+} has a $6s^2$ electronic configuration with ground state $^1S_0$ and the excited state $6s6p$ which splits into the $^3P_0$, $^3P_1$, $^3P_2$ and $^1S_1$ levels. The emission band of Bi^{3+} is typically located in the blue or green, originating from the ligand-field dependent relaxation of $^3P_1 \rightarrow {}^1S_0$.[28–36] Although the absorption band of $^1S_0 \rightarrow {}^3P_1$ is spin-forbidden, it shows reasonably high oscillator strength due to spin–orbit coupling between the $^3P_1$ and the $^1P_1$ level.[12,35] Similar to Zn_2GeO_4, the absorbed energy of Bi^{3+} can probably be transferred to Yb^{3+} through DC processes. Introduction of Bi^{3+} into Zn_2GeO_4:Yb^{3+} is therefore expected to enable broadband activation of Yb^{3+} NIR photoluminescence.

Experimental section

Powder samples and compacted pellets with nominal compositions of $Zn_{1.998-x}GeO_4$:$Yb_{0.002}^{3+}Bi_x^{3+}$ (x = 0, 0.006, 0.02, 0.06 and 0.18 and is the number of Zn^{2+} which is displaced by Bi^{3+} in Zn_2GeO_4) were synthesized through conventional high-temperature solid state reaction. For that, ZnO, GeO_2, Bi_2O_3 and Yb_2O_3 ($\geq$4 N) were used as starting materials. Stoichiometric batches of ~2 g were thoroughly mixed in an agate mortar, pre-calcined at 900 °C for 4 h in air, again ground in an agate mortar, pressed into pellets and finally fired in air at 1300 °C for 12 h.[20] Blank (Zn_2GeO_4) and singly-doped ($Zn_{1.998}GeO_4$:$Bi_{0.02}$) samples were prepared in the same way for reference.

Powder X-ray diffraction (XRD) patterns were obtained on a Siemens Kristalloflex D500 diffractometer over a 2θ range of 10–70°. UV-vis diffuse reflectance (DR) spectra were recorded with a double-beam photospectrometer (Cary 5000) over the spectral range of 200 to 800 nm with 1 nm step size. Static photoluminescence (PL) and PL excitation (PLE) spectra and dynamic decay curves were collected at room temperature with a high-resolution spectrofluorometer (Horiba Jobin Yvon Fluorolog FL3-22), using a static 450 W Xe lamp and a pulsed 75 W Xe flashlamp as excitation sources, respectively. NIR PL was observed with an InP/InGaAs-based thermoelectrically cooled photomultiplier tube (NIR-PMT, Hamamatsu H10330A-75). PLE spectra were measured between 250 to 500 nm with a step size of 1 nm. PL spectra were recorded between 390 and 700, and 930 and 1200 nm with a step size of 1 nm. PLE spectra were corrected over the lamp intensity with a silicon photodiode. PL spectra were corrected with the spectral response of employed PMT.

Results and discussion

Fig. 1a displays *ex situ* powder XRD patterns of as-prepared $Zn_{1.998-x}GeO_4$:$Yb_{0.002}^{3+}Bi_x^{3+}$ for varying values of x. As the major crystal phase in all samples, we identify rhombohedral Zn_2GeO_4 (JCPDS card no. 00-013-0687). A minor amount of secondary $Bi_4(GeO_4)_3$ (cubic I$\bar{4}$3d, JCPDS card no. 01-084-0505) can also be indexed at x > 0.06. The unit cell crystal structure of Zn_2GeO_4 and $Bi_4(GeO_4)_3$ are shown in Fig. 1b and c, respectively. The crystal structure of willemite-type Zn_2GeO_4 belongs to space group $R\bar{3}$ (no. 148). It is comprised of corner-sharing [ZnO_4] and [GeO_4] tetrahedra (Fig. 1b).[20,25] While the incorporation of Bi^{3+} into the crystal lattice is expected to result in a change of lattice

parameters and in decreasing symmetry (assumedly due to the parallel formation of oxygen vacancies which is necessary for charge compensation), we do not observe a notable shift in the diffraction peaks. This indicates the very low solubility of Bi^{3+} ions in Zn_2GeO_4 which can be understood on the basis of the large difference in ionic radii between Bi^{3+} and Zn^{2+} or Ge^{4+}. The ionic radii of Zn^{2+} and Ge^{4+} in fourfold coordination are 0.60 and 0.39 Å, respectively.[37] There is no clear data available on fourfold-coordinated Bi^{3+}, though. For fivefold coordination, it is 0.96 Å, a significant 60% higher than the $^{IV}Zn^{2+}$ radius. The appearance of the secondary crystal phase is a consequence of this low solubility of Bi^{3+} ions in Zn_2GeO_4. Eulytite-type $Bi_4(GeO_4)_3$ is composed of [BiO_6] octahedra and [GeO_4] tetrahedra (Fig. 1c).[38] It is known as scintillator material and – due to the $^{VI}Bi^{3+}$-site – is an excellent host for optically active dopants.[38,39]

Fig. 2 exemplarily shows DR spectra of blank Zn_2GeO_4 and Bi^{3+} (x = 0.02) singly-doped Zn_2GeO_4. The blank Zn_2GeO_4 sample exhibits a broad absorption band in the UV region, *i.e.*, from ~200 to 360 nm. This absorption band can be deconvoluted in at least two contributions: an intense band at ~200–290 nm and a weaker shoulder at ~290–360 nm. The intense absorption band is ascribed to electronic transitions from the valence band to the conduction band of Zn_2GeO_4 host, whereas the origin of the weaker shoulder is not clear.[20] From the absorption edge in UV region at ~263 nm, we estimate a band-gap energy of ~4.71 eV which is good accordance with reported data.[25,40] Addition of Bi^{3+} adds a strong yellow absorption band (originating from the allowed transition of $^1S_0 \rightarrow {}^3P_1$ in trivalent bismuth), shifting the UV-edge to ~450 nm.
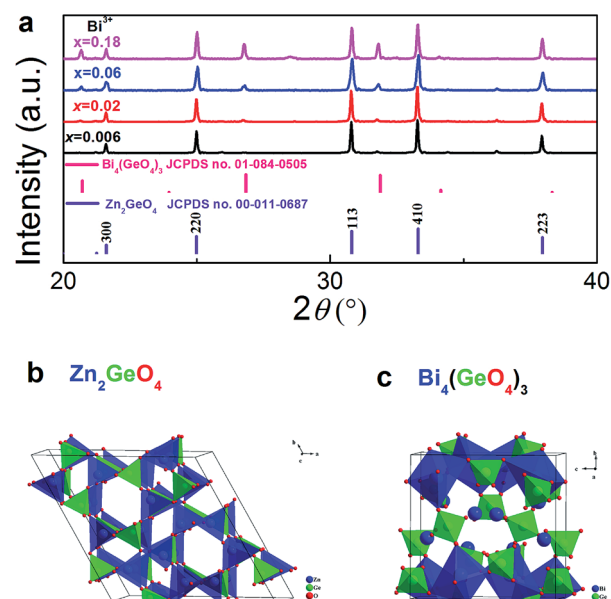

Fig. 1 (a) *Ex situ* powder XRD patterns of $Zn_{1.998-x}GeO_4$:$Yb_{0.002}^{3+}Bi_x^{3+}$ (x = 0, 0.006, 0.02, 0.06 and 0.18) in dependence of Bi^{3+} doping concentration. Tabulated standard diffraction patterns of Zn_2GeO_4 and $Bi_4(GeO_4)_3$ are shown for reference. The unit cell crystal structure of (b) Zn_2GeO_4 and (c) $Bi_4(GeO_4)_3$ with [ZnO_4]/[BiO_6] and [GeO_4] tetrahedra is also shown.

8084 | *J. Mater. Chem. C*, 2014, 2, 8083–8088

This journal is © The Royal Society of Chemistry 2014

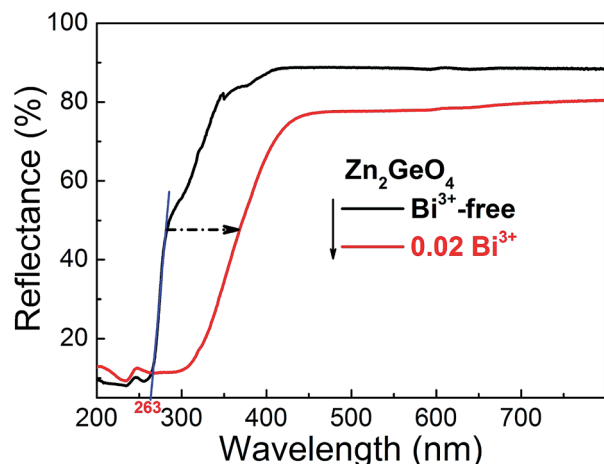**Fig. 2** UV-vis diffuse relectance spectra of blank Zn_2GeO_4 (black line) and Bi^{3+} ($x = 0.02$) singly doped Zn_2GeO_4 (red line). The band gap value of Zn_2GeO_4 is derived by the intersection of tangent (blue line) with abscissa. The blue tangent is shown as a guide for the eye to highlight the band-gap of Zn_2GeO_4.

As already mentioned, Zn_2GeO_4 is a self-activated phosphor. In Fig. 3a and b, we show the room-temperature PLE and PL spectra of blank Zn_2GeO_4. PLE occurs in a strong band from 250 to 280 nm and another, weaker band from 280 to 375 nm, which is consistent with the DR spectra shown in Fig. 2. The excitation maximum locates at ~270 nm which correspond-well with the band gap energy of pure Zn_2GeO_4. Under UV excitation at 270 nm, PL occurs in the spectral region of ~475–625 nm with a maximum at ~540 nm with a full width at half maximum (FWHM) of ~1647 cm^{-1} (~48 nm) (Fig. 3b). This PL band is

assigned to radiative defect-recombination, *i.e.*, a donor ($V_O^{\cdot}$ and Zn_i) and an acceptor defect (V_{Zn}' and ionized V_{Ge}).[27] As for effective PL lifetime $\tau_{1/e}$, we find a range < 3 μs (that is, below the pulse length of the employed Xe flash lamp).

Room-temperature PLE and PL spectra of Yb^{3+} in Yb^{3+} singly-doped Zn_2GeO_4 are provided in Fig. 3c and d. The PLE spectrum is very similar to the spectrum of pure Zn_2GeO_4 (Fig. 3a) and also corresponds to the DR spectrum (Fig. 2), showing the aforementioned two contributions at 250–290 nm and 290–375 nm. This directly evidences PL activation of Yb^{3+} through energy transfer from the Zn_2GeO_4 host. The corresponding NIR PL covers a broad spectral region of 930–1100 nm with a sharp peak at 976 nm and two red-shifted shoulders. The PL spectrum can best be deconvoluted into three Gaussian functions with maxima at 976, 1001 and 1055 nm (as shown in Fig. 3d). Since neither Bi^{3+} nor the Zn_2GeO_4 host are expected to contribute to the NIR emission at this excitation band, the observed NIR PL is assigned to the transition from the lowest stark level of Yb^{3+}:$^2F_{2/5}$ to the three different stark levels of the ground state of Yb^{3+}:$^2F_{2/7}$ (inset of Fig. 3d). The occurrence of Yb^{3+}-related PL after excitation into the conduction band of Zn_2GeO_4 confirms existence of energy transfer from Zn_2GeO_4 to Yb^{3+}.

Fig. 4a–c present room-temperature PLE and PL spectra of Bi^{3+} in $Zn_{1.998-x}GeO_4$:$Yb_{0.002}^{3+}Bi_x^{3+}$ for varying values of x. In the presence of Bi^{3+}, an additional PL band appears in the spectral range of 390 to 500 nm (maximum at 420 nm, FWHM ~4325 cm^{-1}, excitation at 350 nm). This is ascribed to the transition of Bi^{3+}: $^3P_1 \rightarrow {}^1S_0$ (Fig. 4c). The Stokes-shift of this Bi^{3+}-related PL is relatively low, *i.e.*, ~5200 cm^{-1}.[29] With increasing Bi^{3+} concentration, the intensity of the Bi^{3+}-related PL is found to decrease as a result of concentration quenching effect (inset of Fig. 4c).[41,42] The corresponding PLE spectra exhibit two distinct
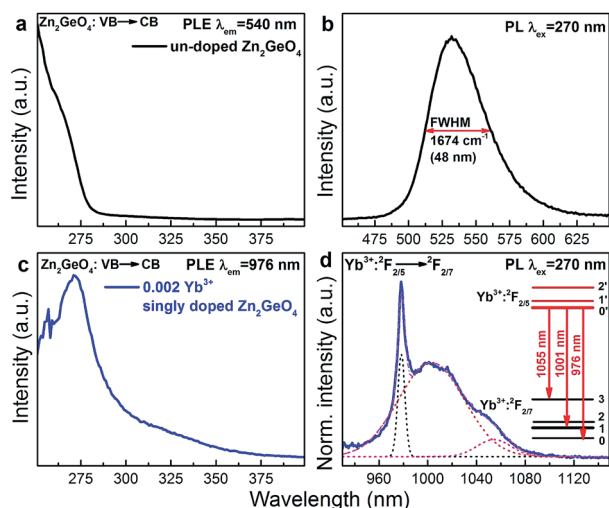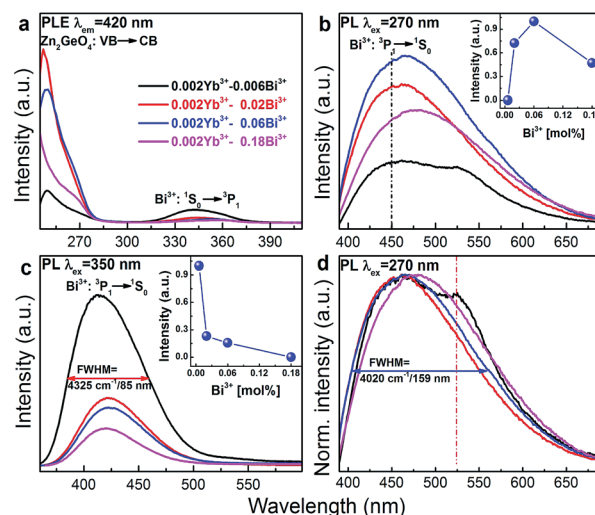

Fig. 3 (a) Room-temperature PLE ($\lambda_{em} = 540$ nm) and (b) PL ($\lambda_{ex} = 270$ nm) spectra for greenish PL in pure Zn_2GeO_4. (c) PLE ($\lambda_{em} = 976$ nm) and (d) PL ($\lambda_{ex} = 270$ nm) spectra of Yb^{3+}:$^2F_{2/5} \rightarrow Yb^{3+}$:$^2F_{2/7}$ emission in Yb^{3+} singly doped Zn_2GeO_4. The inset of (d) presents the Stark splitting energy levels of Yb^{3+} from the best fit of the PL spectrum of Yb^{3+}. The dashed and solid lines in (d) represent the individual Gaussian functions and total fit of the spectra, respectively, as used for deconvolution.

Fig. 4 Room-temperature PLE ($\lambda_{em} = 420$ nm), PL ((b) $\lambda_{ex} = 270$ nm and (c) $\lambda_{ex} = 350$ nm) and (d) normalized PL ($\lambda_{em} = 270$ nm; normalized to the PL peak at 450 nm) spectra of $Zn_{1.998-x}GeO_4$:$Yb_{0.002}^{3+}Bi_x^{3+}$ ($x = 0.006$, 0.02, 0.06 and 0.18) as a function of Bi^{3+} doping concentration. The insets of (b) and (d) show PL peak intensity in $Zn_{1.998-x}GeO_4$:-$Yb_{0.002}^{3+}Bi_x^{3+}$ phosphors *versus* Bi^{3+} doping concentration. The drawn lines in the inset of (b) and (c) are to guide the eye.

bands, *i.e.*, from 250 to 290 nm and from 310 to 390 nm, with peaks at ∼250 and 345 nm, respectively (Fig. 4a). The high-energy part is ascribed to the extrinsic PLE band of the afore-mentioned transition from the valence to the conduction band of Zn_2GeO_4, which suggests the energy transfer from the Zn_2GeO_4 host to Bi^{3+}. The latter contribution is assigned to the intrinsic transition of Bi^{3+}: $^1S_0 \rightarrow {}^3P_1$. Under extrinsic excitation through the Zn_2GeO_4 host (270 nm), the overlapping PL bands the Bi^{3+} active center and the Zn_2GeO_4 host itself can be observed simultaneously with peaks at ∼450 and ∼525 nm, respectively (Fig. 4b and d). The overall PL spectrum therefore spans the very broad spectral region of 390–650 nm with a FWHM of ∼4020 cm^{-1} (∼160 nm). The maximum PL intensity of Bi^{3+}: $^3P_1 \rightarrow {}^1S_0$ is found for $x = 0.06$, whereas PL from the Zn_2GeO_4 host is quenched with increasing concentration of Bi^{3+}, again confirming the occurrence of energy transfer from Zn_2GeO_4 to Bi^{3+}. It is further observed that under extrinsic excitation through Zn_2GeO_4, the PL peak which is attributed to Bi^{3+}: $^3P_1 \rightarrow {}^1S_0$ shifts to longer wavelength, *i.e.*, from ∼420 to 450 nm, as compared to intrinsic excitation of Bi^{3+} centers. This evidences the occurrence of energy transfer from Zn_2GeO_4 to Bi^{3+} through the defect level of Zn_2GeO_4 ($V_O^\cdot$ and Zn_i). As with the intrinsic luminescence from the Zn_2GeO_4 host, the effective lifetime of the Bi^{3+}: $^3P_1 \rightarrow {}^1S_0$ emission is <3 μs.

Room-temperature PLE (monitoring Yb^{3+}: $^2F_{5/2} \rightarrow {}^2F_{7/2}$ PL at 976 nm) and PL (through extrinsic excitation through the Zn_2GeO_4 host at 280 nm and through the Bi^{3+} band at 365 nm, respectively) spectra of $Zn_{1.998-x}GeO_4:Yb_{0.002}{}^{3+}Bi_x{}^{3+}$ are shown in Fig. 5a–c. The PLE bands of the Zn_2GeO_4 host (250 to 315 nm) as well as of the Bi^{3+} active center (345 to 450 nm) can be identified in the PLE spectra of Yb^{3+} (Fig. 5a). This clearly confirms that energy transfer occurs from those entities to Yb^{3+}. The typical Yb^{3+}-related NIR emission can consequently be observed either through excitation of the Zn_2GeO_4 host (270 nm) or through excitation of Bi^{3+}: $^1S_0 \rightarrow {}^3P_1$ (365 nm, Fig. 5b and c). When excited at 270 nm, the introduction of a small amount of Bi^{3+} ($x = 0.06$) strongly enhances the PL intensity of Yb^{3+} (here: more than 12 times, Fig. 5b), whereas higher Bi^{3+} concentration results is quenching of the Yb^{3+}-related PL. Similarly, when excited at 365 nm (*i.e.*, on the Bi^{3+} band), the PL intensity of Yb^{3+} attains a maximum for $x = 0.06$ (Fig. 5c).

Fig. 5d and e represent normalized decay curves of Yb^{3+}: $^2F_{5/2} \rightarrow {}^2F_{7/2}$ PL at $\lambda_{em} = 976$ nm for excitation through the Zn_2GeO_4 host and through Bi^{3+}, respectively. All decay curves deviate from a single-exponential form, which is related to the different mechanisms of energy transfer, and eventually also to the presence of various types of Bi^{3+}-related emission species (where the above-noted optimal dopant concentration coincides with the onset of $Bi_4(GeO_4)_3$ formation (Fig. 1)). The effective lifetime $\tau_{1/e}$ of Yb^{3+}: $^2F_{5/2} \rightarrow {}^2F_{7/2}$ PL increases with increasing Bi^{3+} concentration from ∼90 to 620 μs for excitation through the host (Fig. 5d). When excited through Bi^{3+} species, it first increases from 290 to 510 μs for a Bi^{3+} concentration up to ($x = 0.02$). For higher Bi^{3+} dopant concentration, a saturation is found (Fig. 5e and inset of Fig. 5e).

The overall scheme of spectral conversion in Zn_2GeO_4:-Bi^{3+},Yb^{3+} is illustrated in Fig. 6 and compared to the solar

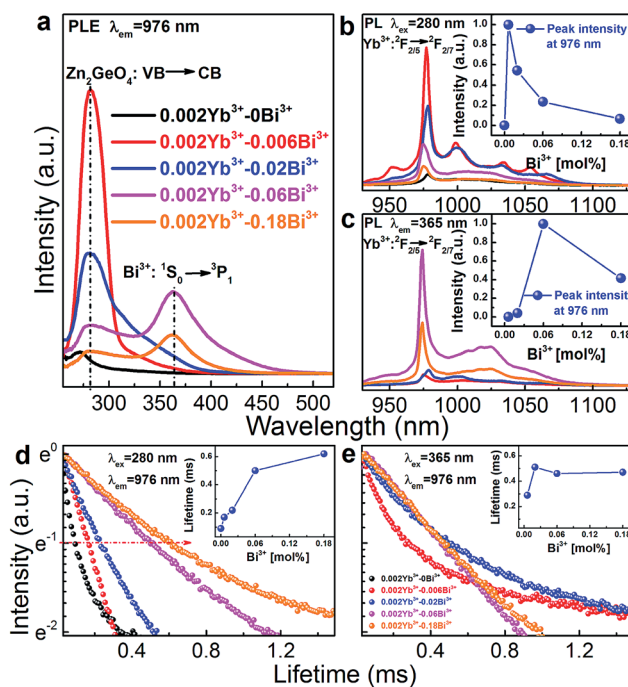**Fig. 5** Room-temperature PLE ($\lambda_{em} = 976$ nm) and PL (upon excitation of (b) Zn_2GeO_4 host at $\lambda_{ex} = 280$ nm and (c) of Bi^{3+} at $\lambda_{ex} = 365$ nm) spectra for NIR PL from Yb^3 emission in $Zn_{1.998-x}GeO_4$:-$Yb_{0.002}{}^{3+}Bi_x{}^{3+}$ ($x = 0$, 0.006, 0.02, 0.06 and 0.18) phosphors as a function of Bi^{3+} concentration. Insets (b) and (c) show PL peak intensity of Yb^{3+} in $Zn_{1.998-x}GeO_4$:$Yb_{0.002}{}^{3+}Bi_x{}^{3+}$ phosphors in dependence of Bi^{3+} concentration. Normalized room-temperature decay curves for NIR PL from Yb^3 at 976 nm under pulsed excitation of at (d) 280 nm (Zn_2GeO_4 host) and (e) 365 nm (Bi^{3+}). Inset of (d) and (e) shows effective lifetime $\tau_{1/e}$ for NIR PL from Yb^3 emission as a function of Bi^{3+} concentration. The lines in the insets of (b), (c), (d) and (e) are guides for the eye.

irradiance spectrum. Without Bi^{3+}, only photons in the spectral region below 350 nm (which accounts for only a small portion of the total solar irradiance) can be harvested. In this case,
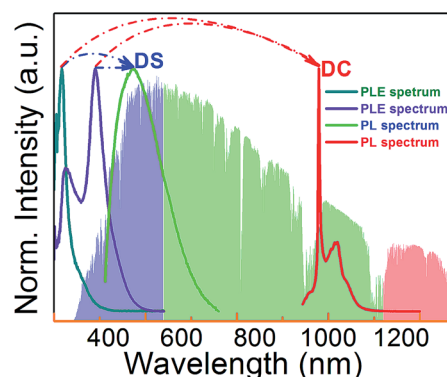

Fig. 6 PLE spectrum of Yb^{3+} in Yb^{3+} singly (cyan line) and Yb^{3+}/Bi^{3+} co-doped (violet line) Zn_2GeO_4, and PL spectrum of $Zn_{1.998-x}GeO_4$:-$Yb_{0.002}{}^{3+}Bi_{0.06}{}^{3+}$ phosphors in visible (green line) and NIR (red line) region under excitation at 280 nm. The standard solar spectrum for air mass 1.5 according to ASTM G173 - 03(2012) is shown in the background for reference.

8086 | *J. Mater. Chem. C*, 2014, **2**, 8083–8088

This journal is © The Royal Society of Chemistry 2014

conversion occurs through intrinsic emission as well as through Yb^{3+} emission centers in the spectral regions of 475–625 nm (green) and 930–1100 nm (NIR). The introduction of Bi^{3+} strongly enhances the spectral harvesting efficiency through extending the absorption band to up to 450 nm. DS PL from both Bi^{3+} and Zn_2GeO_4 then spans a broad region in the blue-to-red spectral range. Through energy transfer from Zn_2GeO_4 to Yb^{3+} *via* Bi^{3+} as well as directly from Bi^{3+} to Yb^{3+}, notable conversion to the NIR region can be obtained. In this way, Yb^{3+}-emission is activated over the excitation region of 250–500 nm.

This process is summarized in Fig. 7 which depicts the energy level diagrams of the Zn_2GeO_4 host together with the Bi^{3+} and Yb^{3+} emission centers. For Yb^{3+} singly-doped Zn_2GeO_4, the electrons are excited from valence to conduction band, leaving hole centers at the valence band under excitation at 270 nm. These defects are subsequently trapped through non-radiative processes.[20,26,27] Their recombination is accompanied by the intrinsic PL emission of the Zn_2GeO_4 host at ∼ twice the energy-gap of Yb^{3+}: $^2F_{7/2} \rightarrow {}^2F_{5/2}$. As a result, besides PL emission, the trapped energy can also be transferred to two neighboring Yb^{3+} entities, resulting in NIR emission at ∼1000 nm. Due to the absence of an intermediate energy level at ∼1000 nm, the energy transfer from Zn_2GeO_4 host to Yb^{3+} is understood as a second order cooperative DC process. With the introduction of Bi^{3+}, the absorption band extends to the blue region. Electrons which are excited into the conduction band of Zn_2GeO_4 can relax to the defect level of Zn_2GeO_4 ($V_O^{\cdot}$ and $Zn_i^{\cdot}$) and then to the excited level of Bi^{3+}: $^3P_1$. Alternatively, the excited electrons at conduction band of Zn_2GeO_4 can directly relax to the excited level of Bi^{3+}: $^3P_1$ through a multi-phonon-assisted relaxation process. At a small Stokes shift of the Bi^{3+}: $^3P_1$ level, DS PL from Bi^{3+} can be observed at an emission energy which is a little bit more than twice the absorption energy of Yb^{3+}: $^2F_{7/2} \rightarrow {}^2F_{5/2}$. Similar to host excitation, also here, energy can be transferred

to two neighboring Yb^{3+} in a cooperative DC process to yield Yb^{3+} emissions at ∼1000 nm. Under excitation at 365 nm, the electrons are excited from the ground state of Bi^{3+}: $^1S_0$ to the excited state of Bi^{3+}: $^3P_1$. The following processes are the same as just described.

Conclusions

In conclusion, we discussed the spectral properties of the high-bandgap semiconductor Zn_2GeO_4 co-doped with Yb^{3+} and Bi^{3+} as a model system for ultra-efficient conversion of the UV-A/blue part of the solar spectrum to the NIR spectral region. We have shown that Yb^{3+}-related PL can be activated through intrinsic absorption of the Zn_2GeO_4 lattice itself, and through Bi^{3+} centers. Energy transfer then occurs *via* cooperative DC from trapped defect states and from the $^3P_1$ level of Bi^{3+}. This results in a strong increase in the absolute intensity of Yb^{3+}-related PL. The material enables ultra-efficient harvesting of UV-A to visible radiation for energy conversion processes which rely on NIR irradiation such at c-Si photovoltaics and various photochemical processes.

Acknowledgements

Notes and references

1 X. Huang, S. Han, W. Huang and X. Liu, *Chem. Soc. Rev.*, 2012, **42**, 173–201.

2 Q. Y. Zhang and X. Y. Huang, *Prog. Mater. Sci.*, 2010, **55**, 353–427.

3 J. de Wild, A. Meijerink, J. K. Rath, W. G. J. H. M. van Sark and R. E. I. Schropp, *Energy Environ. Sci.*, 2011, **4**, 4835–4848.

4 B. M. van der Ende, L. Aarts and A. Meijerink, *Phys. Chem. Chem. Phys.*, 2009, **11**, 11081–11095.

5 L. Wondraczek, M. Batentschuk, M. A. Schmidt, R. Borchardt, S. Scheiner, B. Seemann, P. Schweizer and C. J. Brabec, *Nat. Commun.*, 2013, **4**, 2047.

6 M. Peng and L. Wondraczek, *J. Mater. Chem.*, 2009, **19**, 627–630.

7 Q. Xia, M. Batentschuk, A. Osvet, P. Richter, D.-P. Häder, J. Schneider, C. J. Brabec, L. Wondraczek and A. Winnacker, *Opt. Express*, 2013, **21**, A909–A916.

8 D. Chen, Y. Wang and M. Hong, *Nano Energy*, 2012, **1**, 73–90.

9 T. Trupke, M. A. Green and P. Würfel, *J. Appl. Phys.*, 2002, **92**, 1668–1674.

10 G. Gao and L. Wondraczek, *Opt. Mater. Express*, 2013, **3**, 633–644.

11 D. Yu, S. Ye, M. Peng, Q. Zhang and L. Wondraczek, *Appl. Phys. Lett.*, 2012, **100**, 191911.

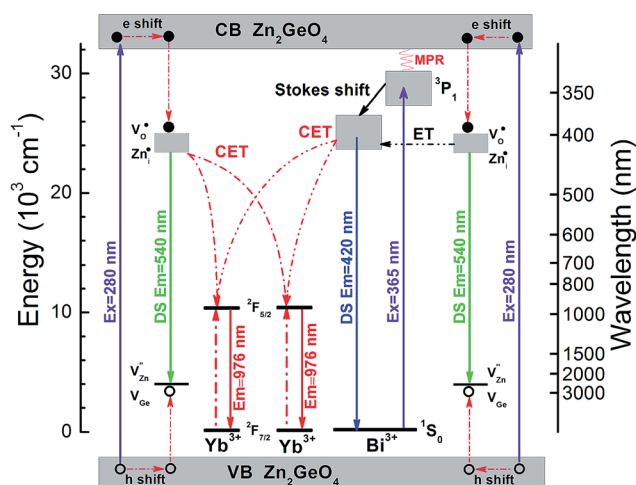12 D. Yu, X. Huang, S. Ye, M. Peng, Q. Y. Zhang and L. Wondraczek, *Appl. Phys. Lett.*, 2011, **99**, 161904.

Fig. 7 Energy level diagrams of Zn_2GeO_4 host, Bi^{3+} and Yb^{3+}, and schematic illustration of the energy transfer mechanisms from the Zn_2GeO_4 host to Yb^{3+}, from the Zn_2GeO_4 host to Yb^{3+} *via* Bi^{3+} and from Bi^{3+} to Yb^{3+} (CET: cooperative energy transfer; ET: energy transfer; MET: multi-phonon-assisted energy transfer).

This journal is © The Royal Society of Chemistry 2014

J. Mater. Chem. C, 2014, **2**, 8083–8088 | **8087**

13 J. Zhou, Y. Teng, S. Zhou and J. Qiu, *Int. J. Appl. Glass Sci.*, 2012, **3**, 299–308.

14 R. Zhou, Y. Kou, X. Wei, C. Duan, Y. Chen and M. Yin, *Appl. Phys. B*, 2012, **107**, 483–487.

15 L. Aarts, B. van der Ende, M. F. Reid and A. Meijerink, *Spectrosc. Lett.*, 2010, **43**, 373–381.

16 J. J. Eilers, D. Biner, J. T. van Wijngaarden, K. Krämer, H.-U. Güdel and A. Meijerink, *Appl. Phys. Lett.*, 2010, **96**, 151106.

17 Q. Y. Zhang, G. F. Yang and Z. H. Jiang, *Appl. Phys. Lett.*, 2007, **91**, 051903.

18 B. M. van der Ende, L. Aarts and A. Meijerink, *Adv. Mater.*, 2009, **21**, 3073–3077.

19 H. Lin, D. Chen, Y. Yu, A. Yang and Y. Wang, *Opt. Lett.*, 2011, **36**, 876–878.

20 G. Gao and L. Wondraczek, *J. Mater. Chem. C*, 2013, **1**, 1952–1958.

21 Y. Li, J. Wang, W. Zhou, G. Zhang, Y. Chen and Q. Su, *Appl. Phys. Express*, 2013, **6**, 082301.

22 X. Y. Huang and Q. Y. Zhang, *J. Appl. Phys.*, 2010, **107**, 063505.

23 X. Wei, S. Huang, Y. Chen, C. Guo, M. Yin and W. Xu, *J. Appl. Phys.*, 2010, **107**, 103107.

24 M. Balestrieri, G. Ferblantier, S. Colis, G. Schmerber, C. Ulhaq-Bouillet, D. Muller, A. Slaoui and A. Dinia, *Sol. Energy Mater. Sol. Cells*, 2013, **117**, 363–371.

25 C. Yan, N. Singh and P. S. Lee, *Appl. Phys. Lett.*, 2010, **96**, 053108.

26 G. Anoop, K. M. Krishna and M. K. Jayaraj, *J. Electrochem. Soc.*, 2008, **155**, J7–J10.

27 Z. Liu, X. Jing and L. Wang, *J. Electrochem. Soc.*, 2007, **154**, H500–H506.

28 G. Blasse and B. C. Grabmaier, *Luminescent materials*, Springer-Verlag, 1994.

29 G. Blasse and A. Bril, *J. Chem. Phys.*, 1968, **48**, 217–222.

30 M. Peng, G. Dong, L. Wondraczek, L. Zhang, N. Zhang and J. Qiu, *J. Non-Cryst. Solids*, 2011, **357**, 2241–2245.

31 M. Ilmer, B. C. Grabmaier and G. Blasse, *Chem. Mater.*, 1994, **6**, 204–206.

32 F. Kang, X. Yang, M. Peng, L. Wondraczek, Z. Ma, Q. Zhang and J. Qiu, *J. Phys. Chem. C*, 2014, **118**, 7515–7522.

33 W. Xu, M. Peng, Z. Ma, G. Dong and J. Qiu, *Opt. Express*, 2012, **20**, 15692–15702.

34 N. Niu, F. He, S. Gai, C. Li, X. Zhang, S. Huang and P. Yang, *J. Mater. Chem.*, 2012, **22**, 21613–21623.

35 U. Rambabu and S.-D. Han, *Ceram. Int.*, 2013, **39**, 701–708.

36 M. Peng, B. Sprenger, M. A. Schmidt, H. Schwefel and L. Wondraczek, *Opt. Express*, 2010, **18**, 12852–12863.

37 R. D. Shannon, *Acta Crystallogr., Sect. A: Cryst. Phys., Diffr., Theor. Gen. Crystallogr.*, 1976, **32**, 751–767.

38 R. Nitsche, *J. Appl. Phys.*, 1965, **36**, 2358–2360.

39 Y. T. Arslanlar, Z. Kotan, R. Kibar, A. Canımoğlu and N. Can, *Spectrosc. Lett.*, 2013, **46**, 590–596.

40 Q. Liu, Y. Zhou, J. Kou, X. Chen, Z. Tian, J. Gao, S. Yan and Z. Zou, *J. Am. Chem. Soc.*, 2010, **132**, 14385–14387.

41 G. Gao, R. Meszaros, M. Peng and L. Wondraczek, *Opt. Express*, 2011, **19**, A312–A318.

42 G. Gao, S. Reibstein, E. Spiecker, M. Peng and L. Wondraczek, *J. Mater. Chem.*, 2012, **22**, 2582–2588.

8088 | *J. Mater. Chem. C*, 2014, **2**, 8083–8088

This journal is © The Royal Society of Chemistry 2014